Journal of Structural Geology 98 (2017) 67–82

Contents lists available at ScienceDirect

Journal of Structural Geology

journal homepage: www.elsevier.com/locate/jsg

# LiDAR, UAV or compass-clinometer? Accuracy, coverage and the effects on structural models

Adam J. Cawood [a, *], Clare E. Bond [a], John A. Howell [a], Robert W.H. Butler [a], Yukitsugu Totake [a, b]

[a] Department of Geology and Petroleum Geology, School of Geosciences, University of Aberdeen, Meston Building, Kings College, Aberdeen, AB24 3UE, UK
[b] Technical Resources Unit, Technical Division, INPEX Corporation, Tokyo, 107-6332, Japan

ARTICLE INFO

*Article history:*
Received 12 December 2016
Received in revised form
10 April 2017
Accepted 19 April 2017
Available online 20 April 2017

*Keywords:*
LiDAR
Structure from motion
UAV
Virtual outcrop
Structural model

ABSTRACT

Light Detection and Ranging (LiDAR) and Structure from Motion (SfM) provide large amounts of digital data from which virtual outcrops can be created. The accuracy of these surface reconstructions is critical for quantitative structural analysis. Assessment of LiDAR and SfM methodologies suggest that SfM results are comparable to high data-density LiDAR on individual surfaces. The effect of chosen acquisition technique on the full outcrop and the efficacy on its virtual form for quantitative structural analysis and prediction beyond single bedding surfaces, however, is less certain. Here, we compare the accuracy of digital virtual outcrop analysis with traditional field data, for structural measurements and along-strike prediction of fold geometry from Stackpole syncline. In this case, the SfM virtual outcrop, derived from UAV imagery, yields better along-strike predictions and a more reliable geological model, in spite of lower accuracy surface reconstructions than LiDAR. This outcome is attributed to greater coverage by UAV and reliable reconstruction of a greater number of bedding planes than terrestrial LiDAR, which suffers from the effects of occlusion. Irrespective of the chosen acquisition technique, we find that workflows must incorporate careful survey planning, data processing and quality checking of derived data if virtual outcrops are to be used for robust structural analysis and along-strike prediction.


## 1. Introduction

Virtual outcrops are an important source of information, from which a wide variety of geological data can be derived. These detailed 3D reconstructions of outcrop geology are applied to a broad range of studies, including sedimentology and stratigraphy (e.g., Hodgetts et al., 2004; Enge et al., 2010; Fabuel-Perez et al., 2010; Eide and Howell, 2014; Rarity et al., 2014; Rittersbacher et al., 2014), reservoir modelling (e.g., Enge et al., 2007; Rotevatn et al., 2009; Buckley et al., 2010), and structural geology (e.g., Seers and Hodgetts, 2014; Bistacchi et al., 2015, among others). Light Detection and Ranging (LiDAR) has been the principal acquisition technique for deriving virtual outcrops in the last decade (e.g., Pringle et al., 2006; Buckley et al., 2008; Jones et al., 2009), though acquiring this type of detailed 3D spatial data requires expensive instrumentation and significant knowledge of processing workflows. The recent availability of ready-to-use small Unmanned Aerial Vehicles (UAVs) and the advent of Structure from Motion (SfM) i.e. digital photogrammetry software, has opened-up virtual outcrops to a growing number of Earth scientists. This technique provides the ability to use unreferenced, overlapping images of a structure to semi-automatically generate a 3D reconstruction, easily and without the expense and specialist knowledge required for LiDAR acquisition and processing (James and Robson, 2012). The combination of these factors coupled with the advantage of synoptic aerial survey positions and efficient, rapid surveying afforded by UAVs has seen these techniques gain much popularity in the Earth Science in recent years (Mancini et al., 2013; Bemis et al., 2014; Vasuki et al., 2014; Clapuyt et al., 2016). The aim of this paper is to assess virtual outcrop generation methodologies, the accuracy and reliability of these reconstructions, and the impacts for structural analysis when using these digital datasets, based on a single case study.

The validity of using virtual outcrops to make predictions of the subsurface has been addressed by a number of workers (e.g., Jones et al., 2004; Gillespie et al., 2011; Gold et al., 2012). The accuracy

* Corresponding author.
*E-mail address:* adam.cawood@abdn.ac.uk (A.J. Cawood).

http://dx.doi.org/10.1016/j.jsg.2017.04.004
0191-8141/

and precision of virtual outcrops was found to be critical if geological models derived from them are to make reliable predictions and decisions (García-Sellés et al., 2011; Martín et al., 2013; Tavani et al., 2014). As such, a number of studies have addressed the efficacy of LiDAR derived surface reconstructions in Earth science applications, across a multitude of scales (Jones et al., 2009; Assali et al., 2014; Casini et al., 2016). These studies found that LiDAR provides high accuracy reconstructions, resolvable to mm scales. Similarly, work has been done to test SfM reconstructions with reference to geological problems (e.g., Sturzenegger and Stead, 2009; James and Robson, 2012; Westoby et al., 2012), generally against detailed 3D LiDAR and differential Global Positioning Systems (dGPS) datasets. These studies found that SfM yields acceptable surface reconstructions, albeit with less consistency than those generated by LiDAR. Inaccuracies in SfM datasets include point-cloud 'doming' (James et al., 2017), greater inaccuracies at model edges (e.g., James and Robson, 2012), and failure of automated feature matching due to lack of discernible features in imagery.

The specific focus of this study is whether the known accuracy of LiDAR data automatically results in a better, more reliable geological model when compared with SfM, using data acquired at a single site. Furthermore, we assess whether greater coverage afforded by UAV compensates for instances of lower accuracy and reconstruction reliability if the entire virtual outcrops, rather than isolated patches, are used as a primary source of data for model building. Thus the specific aims of this study are: (1) to assess the efficacy of terrestrial LiDAR, terrestrial SfM (TSfM) and aerial SfM (ASfM) to accurately reconstruct geological surfaces over an entire 3D outcrop, testing the validity of using virtual bedding surfaces for extracting structural data; (2) to evaluate the effects of acquisition method and survey design on the accuracy and reliability of surface reconstructions and coverage of virtual outcrops; (3) to quantify the influence of these factors on geological model building and along-strike predictions of geometry.

Manual and digital compass-clinometer data were used to compare virtual outcrops generated using terrestrial LiDAR, TSfM and ASfM, at a fold structure in SW Wales. Using our direct measurements and derived orientation data from the three virtual outcrops, separate geological models were built and compared. Finally, dGPS data was used to determine the effects of direct georeferencing on the spatial accuracy of the datasets. This paper highlights potential sources of error and inaccuracies introduced during data acquisition and processing and the effects on the reliability of resultant structural measurements. Based upon these results, the impact of the various acquisition methods on along-strike prediction of fold geometry and hinge placement is discussed. Consequently, the implications for survey design and quality checking of data are considered when creating virtual outcrops for structural analysis and prediction.

## 2. Study site

The classic Stackpole Quay syncline (Fig. 1), a photograph of which appeared in the first issue of this publication (Hancock, 1979), is situated on the southeastern edge of the Pembroke Peninsula, West Wales (Fig. 2 and 3D model, supplementary materials). The structure is composed of folded Visean carbonates of the Pembroke Limestone group, and lies close to the northern limit of Variscan deformation (Fig. 2b) in Britain (Dixon, 1921; Hancock, 1964; British Geological Survey, 1996; Downes, 2002). This syncline is an upward-facing fold, contains a sub-vertical axial surface, and a shallowly ENE plunging fold axis (Hancock, 1964).

Stackpole Quay was chosen for this study, as it has a number of features suitable for a comparison of surveying technologies and

**Fig. 1.** Stackpole Quay syncline, SW Wales. After Hancock (1979), as on the cover to the first issue of the Journal of Structural Geology.

methods. Primarily, the 3D nature of the outcrop and continuity of bedding around it allows bedding orientation measurements to be made across the syncline hinge and limbs, at multiple locations along strike (Fig. 2c). The limited outcrop size (47 m × 24 m x 14 m) also enables a rapid and comprehensive survey of the structure, using the chosen acquisition methods (Fig. 2). Notwithstanding its coastal setting, convenient vantage points exist for viewing the structure, and direct access onto the outcrop is possible for collection of structural measurements.

## 3. Fieldwork & instrumentation

The five methodologies used for primary data acquisition are:

(1) Traditional compass-clinometer for direct measurement of bedding dip and dip azimuth
(2) Digital compass-clinometer app for a portable tablet for direct measurement of bedding dip and dip azimuth
(3) Terrestrial LiDAR scans with simultaneous acquisition of digital images for virtual outcrop generation and texturing
(4) Terrestrial (handheld) acquisition of digital photographs for SfM reconstruction (TSfM) for virtual outcrop generation
(5) Aerial acquisition of images by UAV for construction of virtual outcrops using SfM (ASfM)

In addition to these five methods, a differential Global Positioning System (dGPS) was used to acquire precisely located points around the outcrop, allowing co-registration of datasets and calibration of models. LiDAR scan station positions, TSfM acquisition points and dGPS measurement locations provided in Fig. 2a. A summary of the data acquisition, processing and pre-interpreted datasets is provided in Table 1.

### 3.1. Direct measurements of dip and dip azimuth

#### 3.1.1. Traditional compass-clinometer survey

Orientations of bedding surfaces on the structure were collected using a traditional handheld Suunto compass-clinometer. Experienced users of handheld compass-clinometers of this type are reckoned to achieve measurement accuracy within 1° on compass bearings and 2° on dip measurements. These values fall well within

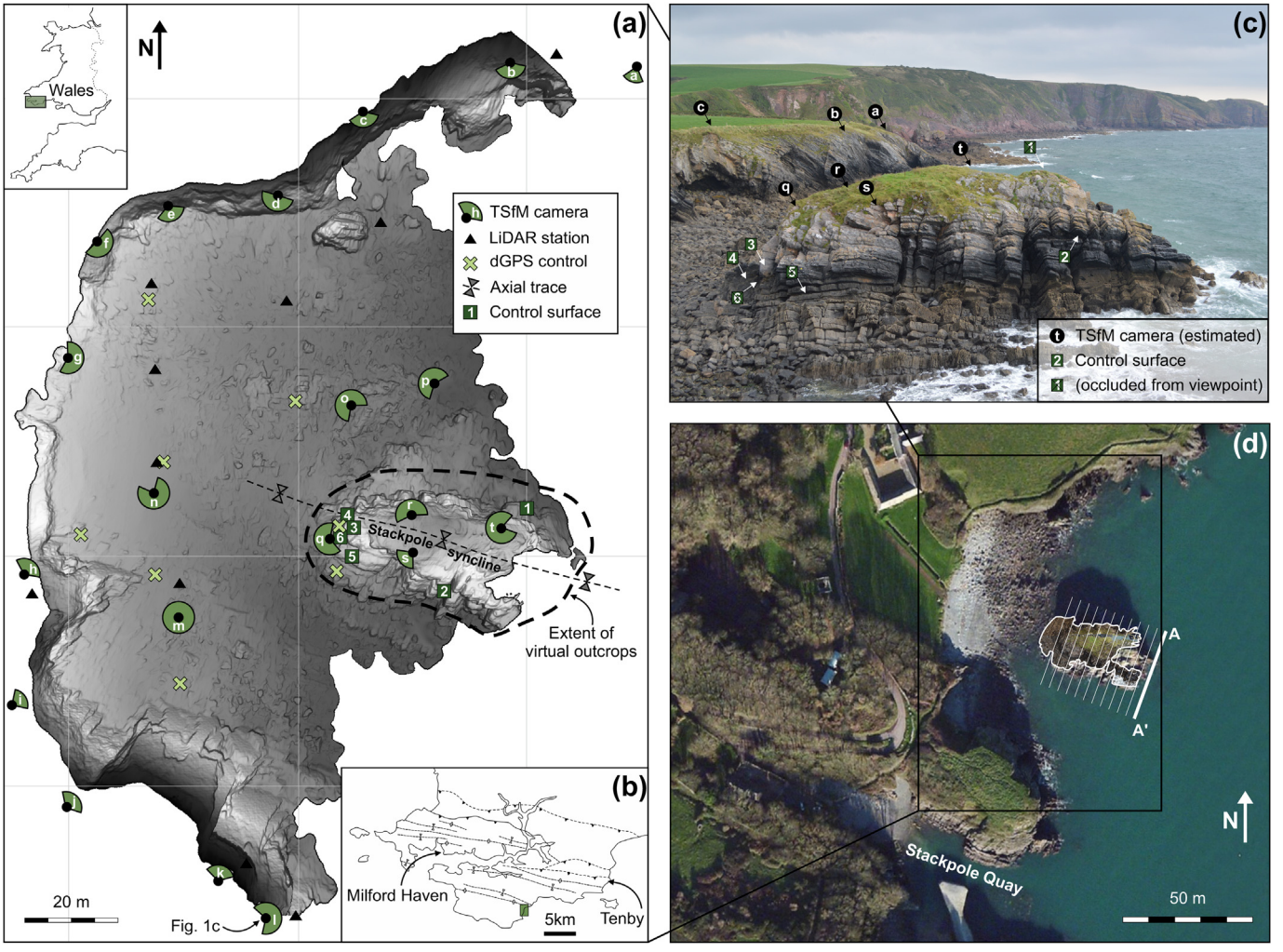


**Fig. 2.** Location and morphology of the study site. (a) Survey map of study site with orthorectified digital elevation model, location of survey stations and extent of virtual outcrop. Inset (top left) showing regional location of site, with shaded box corresponding to (b) summary structural map of Variscan features in Pembrokeshire (after Coward and Smallwood, 1984). Shaded box in (b) corresponds to area of interest. (c) Field photograph of the Stackpole syncline, looking NNE, from camera position (l) on survey map. Boxed letters denote estimated camera positions in image, corresponding to those marked on survey map. (d) Satellite imagery of study area with co-registered LiDAR virtual outcrop (outlined in white). Inset box corresponds to area in Fig. 2a. Section lines used to quantify along-strike variation represented by white traces (Fig. 10). Thick white section line corresponds to Fig. 9.

the range of variability of bedding orientations on single surfaces at Stackpole, and as such this method was assumed to be the 'accurate' base dataset against which the virtual outcrop bedding plane dip and dip azimuths were compared. The locations of orientation measurements were derived from map reading (by author Cawood) and recorded on a 1:500 paper version of the digital Ordnance Survey map of the study area. Subsequent to the data collection, the orientation data and their 3D coordinates were digitized to allow for compilation and comparison with the digital datasets.

#### 3.1.2. Digital compass-clinometer survey

FieldMove, a digital compass-clinometer and notebook package for portable devices (version 1.2.2, 2016) by Midland Valley on iPad Air (3G), was used for digital acquisition of bedding orientations. Automatic positioning of measurements was achieved within the app using the iPad's integrated GPS unit, directly onto preloaded satellite imagery. Accuracy of iPad measurement positioning was generally estimated to be within 3 m of location, in agreement with published data (Lee et al., 2015). On occasion the app mislocated data points (by failing to update GPS co-ordinates) and these were manually corrected, in the app, during field acquisition. The accuracy of FieldMove and other digital compass-clinometer apps on Android devices has been addressed in recent work (Novakova and Pavlis, 2017), but no systematic study of measurement accuracy is available for FieldMove 1.2.2 on iPad Air. According to Midland Valley (2015), FieldMove compass-clinometer measurements on iPad tablets have accuracies to within 5° for compass bearings and 'very good' clinometer accuracy, with results from Apple devices displaying greater reliability than Android or Windows counterparts. During the digital compass-clinometer survey, measurements were regularly monitored and compared with traditional compass-clinometer measurements, in accordance with recommended workflows (e.g. Novakova and Pavlis, 2017).

### 3.2. Remotely acquired data

#### 3.2.1. LiDAR survey

A fully portable, tripod mounted RIEGL VZ-2000 laser scanner was used to scan the study site. Attached to the laser scanner was a Nikon D80 DSLR (10.6 Megapixel) with 50 mm fixed focal length lens for digital image acquisition to texture the 3D LiDAR model. LiDAR scanning followed normal methodologies applied to Earth science applications, with consideration given to sufficient scan overlap and correct scanner positioning to minimize scan occlusion (Bonnaffe et al., 2007; Buckley et al., 2008). The VZ-2000 has a range of over 2 km and acquisition rates of up to 400,000 measurements per second, with each data point assigned local, Cartesian *x,y,z* coordinates (RIEGL, 2015). Ten scans from positions around the outcrop were performed (Fig. 2a), in conjunction with the acquisition of images using the calibrated Nikon D80. Quoted range measurement precision and accuracy of the RIEGL VZ-2000 are 5 mm and 8 mm respectively at 150 m range. GPS survey information to initialise absolute and relative LiDAR scan registration was provided by an integrated single channel GPS receiver and inclination sensors on-board the VZ-2000 scanner, allowing coarse registration of point-clouds during processing.

#### 3.2.2. Terrestrial structure from motion (TSfM) survey

A 24 Megapixel, Nikon D3200 camera was used for terrestrial image acquisition, at a fixed focal length of 26 mm (35 mm equivalent focal length of 39 mm). Images were acquired in auto mode to account for changes in lighting and distance from the structure: exposure times in the image dataset range from 1/100 s to 1/500 s, with ISO values of 100–400. As this survey encompassed Stackpole syncline and the adjacent Stackpole Quay, the original dataset comprised 724 images from 27 camera positions. Only those that included Stackpole syncline or the immediate surroundings were selected for virtual outcrop construction. This procedure resulted in a reduced dataset of 446 images from 20 camera positions used for SfM alignment and virtual outcrop generation (Fig. 2a).

Local topography around the study site and the presence of open sea on the east side of the structure limited the availability of stable camera positions and thus did not allow full coverage of the outcrop (Fig. 2c) in terrestrially acquired images. Camera positions were, however, selected during fieldwork to maximise coverage, synoptic viewpoints and convergent imagery of the study site, where possible, in accordance with workflows laid out by a number of authors (Sturzenegger and Stead, 2009; Westoby et al., 2012; Fonstad et al., 2013). Average ground-pixel resolution for the 402 images utilized for SfM reconstruction was 7.48mm/pixel (Table 1).

#### 3.2.3. Aerial structure from motion (ASfM) survey

This survey was conducted with a DJI Phantom 3 Advanced UAV.

**Table 1**
Summary of data collection, processing and pre-interpretation datasets.

| Technique | Traditional | Digital compass clino | LiDAR | TSfM | ASfM | dGPS |
|---|---|---|---|---|---|---|
| Instrument | Compass clinometer | Fieldmove app on iPad Air | RIEGL VZ-2000 & Nikon D100 | Nikon D3200 & camera pole | DJI Phantom 3 Advanced & on-board camera | Leica VIVA RTK GNSS |
| Instrument resolution | – | – | (0.0015°) Scale dependant | 24 Megapixel | 12 Megapixel | 9-15 mm accuracy (3D, in this survey) |
| Approximate cost (USD) of equipment[g] | $60 | $500 | $100,000 | $600 | $1800 | $40,000 |
| Acquisition time (hrs.) | 8 | 3 | 5 (10 scans) | 1.5 | 0.5 (flight & preparation) | 1 |
| Processing time (hrs.) | 3[a] | – | 35[b] | 8[c] | 8[c] | – |
| Raw dataset | 425 measurements | 625 measurements | $1.23 \times 10^8$ points | 446 digital images (402)[d] | 202 digital images (198)[d] | 106 spatial measurements |
| Processed pointcloud size | – | – | $4.7 \times 10^6$[e] | $1.8 \times 10^5$[f] | $2.6 \times 10^6$[f] | – |
| Pointcloud resolution (mm) | – | – | 4 | 12 | 7 | – |
| Mesh face count | – | – | $4 \times 10^6$ | $6.7 \times 10^5$ | $2.3 \times 10^6$ | – |

[a] Data digitization.
[b] Significant/continuous user input.
[c] Largely automated processing.
[d] Matched images in brackets.
[e] Decimated LiDAR point-cloud.
[f] SfM derived pointcloud.
[g] Includes processing software, where relevant.

No upgrades or modifications were made to the UAV prior to the field campaign. Flights were piloted manually, without the use of a flight planning package. Automatic acquisition of digital images at 5 s intervals was performed with the on-board, 12 Megapixel camera at automatic exposure levels. A single 15-min flight over the study area, generated 202 digital images (Fig. 3a) of the outcrop with average image ground-pixel resolution of 6.24mm/pixel. The on-board GPS receiver provided approximate coordinates of each image acquisition point during the survey flight (Fig. 3b).

### 3.3. Differential Global Positioning System survey (dGPS) survey

A spatial survey (Fig. 2a) was conducted with a Leica Viva dGPS system with Real Time Kinematic (RTK) corrections received by radio link, allowing measurement of point locations with 3D accuracy, in this survey, of 0.009–0.015 m. Setting up a GPS base station 20 m from the structure and conducting the survey with a rover unit enabled achieving this accuracy. The justifications for including a dGPS in our survey methodology are threefold:

- *To precisely define Ground Control Point (GCP) positions* in the survey area, and incorporate them into the TSfM processing workflow (Section 4.2.1). GCPs were located during fieldwork according to protocols set out by a number of authors to ensure an accurately georeferenced virtual outcrop (Bitelli et al., 2004; Bates et al., 2008; Assali et al., 2014; Bistacchi et al., 2015).
- *To ease compilation of all data into a single oriented geometrical framework* (see Section 4.4).
- *To test the efficacy of direct georeferencing* of point-clouds and virtual outcrops using on-board GPS instruments for terrestrial LiDAR and ASfM surveys. This latter analysis was achieved by recording 108 positions on the structure, specific to individual bedding surfaces. This protocol enabled an assessment of the positional accuracy of virtual outcrops generated without GCPs (Section 4.4.1).

## 4. Data processing and georeferencing

### 4.1. LiDAR

Following acquisition of field data, the pre-processed LiDAR

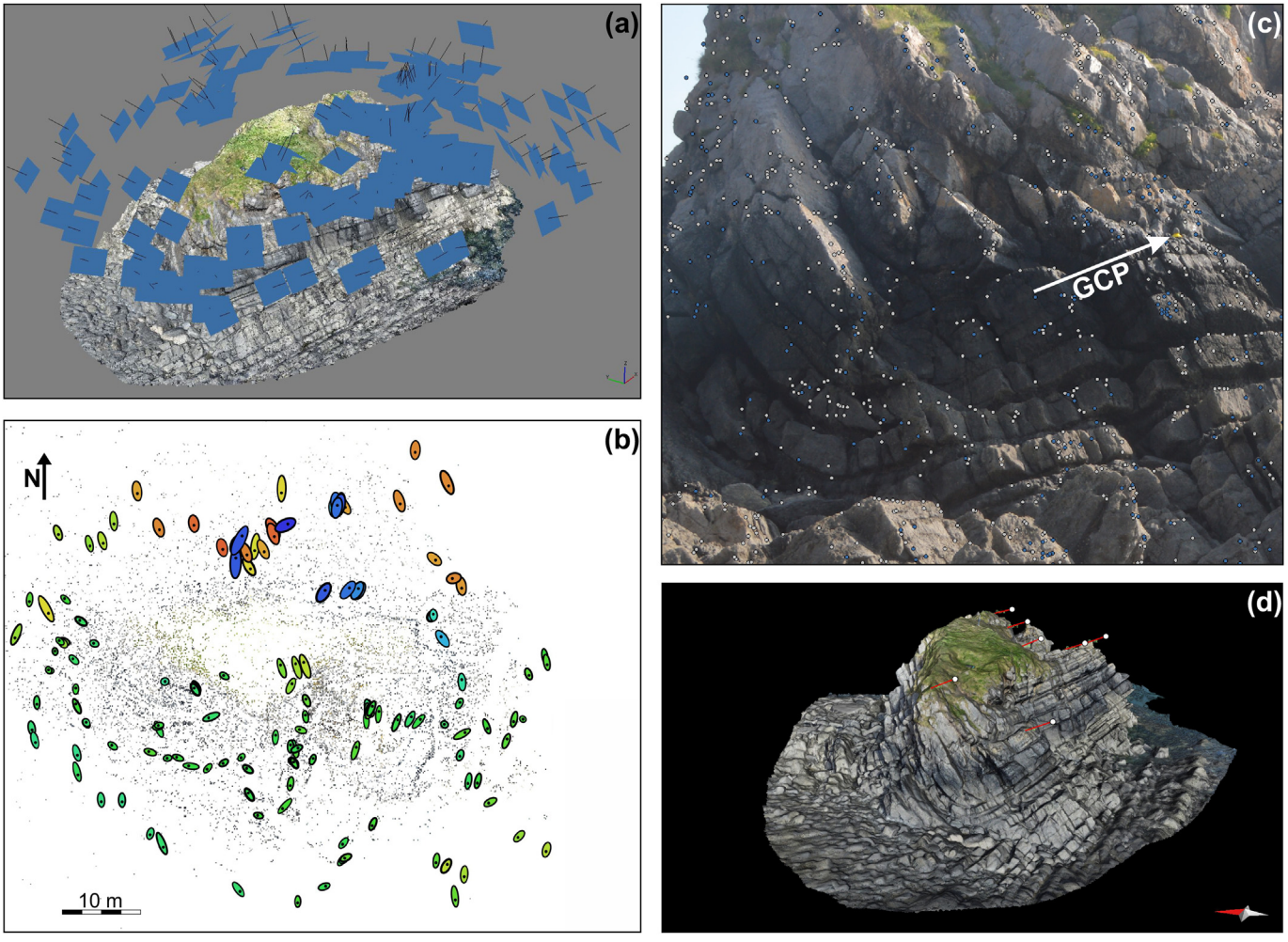


**Fig. 3.** SfM acquisition and processing steps. (a) Image acquisition points for a single UAV flight, highlighting the ability to obtain convergent imagery of Stackpole Quay syncline. Image coordinates recorded during acquisition, with camera orientations estimated during ASfM processing stage (Section 4.2.2). (b) Estimated camera locations and error estimates from UAV acquisition. X and Y errors represented by size and shape of ellipses. (c) Features automatically detected during TSfM processing in *Photoscan*, from which 3D coordinates may be estimated. Features used to construct 3D tie point network marked by dark circles and lighter grey points not used for reconstruction. White arrow marks position of ground control point laid out and recorded during acquisition of TSfM imagery. See section 3.2.2 and 4.2.1 for details of acquisition and processing. (d) Visual representation of applied corrections to direct georeferencing of ASfM virtual outcrop (see Table 2 for applied corrections). Spheres represent RTK dGPS measurement points. Applied translation vectors of virtual outcrop shown by lines (Section 4.4.1). A 3D version of the ASfM virtual outcrop is provided in supplementary materials and at: https://sketchfab.com/models/9e4466b58d844c2bab791009f0766706 (for annotated version).

point-clouds and digital images required a number of processing steps to generate a final virtual outcrop. Buckley et al. (2008) provide a detailed review about the processing procedure for LiDAR datasets acquired for use in the Earth Sciences. Absolute and co-registration of the point-clouds generated from the individual scan stations was achieved using *RiScan Pro* (RIEGL GmbH), with coordinates provided by on-board GPS measurements during acquisition. Subsequent to coarse, manual co-registration of point-clouds (from 10 LiDAR scans), filtering and decimation of point-cloud data was performed to reduce point redundancy from overlapping scans and adverse effects caused by the presence of vegetation. An iterative closest points algorithm was used in *RiScan Pro* to automatically align point-clouds after filtering and decimation. A 'least square fitting' calculation was performed to align a total of 9246 points from the 10 point-clouds. Overall standard deviation of distances between all used pairs of tie-points was quoted in *RiScan Pro* as 0.0095 m.

### 4.2. Structure from motion (SfM)

The fundamental process of SfM is a feature-detection-and-description algorithm by which common features or textures in overlapping images are identified (Seitz et al., 2006). After detection of matched features (Fig. 3c), they are assigned 3D coordinates and iteratively the software automatically constructs a 3D network of matched or tie-points. Subsequent to the creation of the 3D tie-point network, a dense cloud is generated to populate the space between tie-points, by a MVS (multi-view stereo) algorithm. This algorithm essentially functions by searching pixel grids within images, selecting the best matches and generating points in 3D space (e.g. Furukawa and Ponce, 2010; Seitz et al., 2006; Hirschmuller, 2008). Estimated achievable precision of SfM-derived point coordinates is controlled by: (1) number of overlapping images in which the feature of interest appears; (2) mean distance from camera to target; (3) distance between camera centres relative to the object of interest, i.e. the angle of image convergence on the scene; (4) principal distance of camera, a measurement similar to focal length; and (5) the precision of image measurements and reconstruction parameters (James and Robson, 2012).

Generation of tie-point networks and dense point-clouds to derive virtual outcrops was performed using *Agisoft PhotoScan Professional 1.1.6* (*PhotoScan*), from protocols set out by a number of authors (Javernick et al., 2014; Tavani et al., 2014; James et al., 2017). Processing parameters in *Photoscan* for ASfM and TSfM datasets were identical, to allow direct comparison. Images were aligned at 'high' accuracy, with generic pair pre-selection enabled, and default key and tie point limits of 40,000 and 1000 respectively. Dense cloud construction was set at 'high quality' with depth filtering set to 'aggressive', improving the accuracy of automatically estimated point coordinates.

#### 4.2.1. Terrestrial Structure from motion (TSfM)

A dense point-cloud of $1.8 \times 10^5$ points was generated from a raw dataset of 446 terrestrial images (402 of which were automatically aligned), using the stated parameters in *Photoscan.* As locations of camera positions were recorded using a consumer-grade GPS, this information was not included in the processing workflow in *Photoscan.* High precision dGPS measurements of GCPs (Fig. 2c) were, however, defined during processing, following established procedures (e.g. Javernick et al., 2014) to allow precise georeferencing of the dataset.

#### 4.2.2. Aerial structure from motion (ASfM)

The 202 images taken in the single 15-min UAV flight were automatically geotagged during acquisition (Fig. 3a). *PhotoScan* automatically utilized this information during the SfM processing to enhance the image matching process and constrain estimates of camera locations. Processing time was consequently reduced, and direct georeferencing of point-clouds was enabled by using the global coordinate system WGS 1984. This direct georeferencing can be overridden or supplemented during processing by defining GCPs, as in our terrestrial photogrammetry dataset. However, to allow estimation of the accuracy of auto-registration, this protocol was not used. Efficacy of direct georeferencing by PhotoScan and necessary post-processing corrections is addressed in Section 4.4.1.

### 4.3. Point-cloud subsampling and meshing

To obtain spatially homogenous point-cloud data, each point-cloud created by the three methods was subsampled using *Cloud-Compare*, an open-source software package for 3D point processing (Table 1). Semi-automated triangulation and generation of 3D mesh surfaces from processed point-clouds was done using *Innovmetric PolyWorks.* Any obvious meshing artefacts and holes were manually corrected in *PolyWorks*. Identical procedures were followed for each point-cloud in *PolyWorks* to allow comparison of the final outcomes. Mesh face counts are provided in Table 1. Subsequent to meshing, texturing by projection of images was carried out within RiScan Pro and Agisoft PhotoScan for the LiDAR and photogrammetric datasets, respectively. As the focus of this study is the geometrical accuracy of virtual outcrops, rather than quality of texturing and photorealism, this step was performed at a relatively low resolution (Fig. 3d) to allow easier handling of data during interpretation. Finally, the three separate virtual outcrops were co-registered in the digital environment, using the spatial data collected by dGPS and on-board LiDAR scanner and UAV instruments. Table 1 provides a summary of pre and post processed point-clouds and resultant meshes.

### 4.4. Spatial co-registration of datasets

Prior to any structural analysis of the virtual outcrops, or of the directly collected field data, the datasets needed to be co-registered

**Table 2**
Corrections applied to directly georeferenced ASfM virtual outcrop from dGPS measurements.

| | | GCP1 | GCP2 | GCP3 | GCP4 | GCP5 | GCP6 |
|---|---|---|---|---|---|---|---|
| Applied corrections[a] | x component (m) | −1.16 | −1.06 | −0.95 | −1.02 | −1.21 | −1.07 |
| | y component (m) | −2.63 | −2.57 | −2.46 | −2.49 | −2.37 | −2.43 |
| | z component (m) | +0.79 | +0.1 | +1.11 | +1.03 | +1.32 | +0.78 |
| Displacement vector[b] | (m) | 2.99 | 2.94 | 2.86 | 2.88 | 2.96 | 2.77 |
| | azimuth (°) | 23.9 | 19.8 | 21.1 | 22.4 | 26.1 | 23.7 |
| | plunge (°) | 15.3 | 21.4 | 23.11 | 20.1 | 27.2 | 16.3 |

[a] x = east; y = north, z = elevation.
[b] Displacement vector calculated from x,y and z components of applied corrections.

into a single oriented geometrical frame. First, individual compass-clinometer dip and dip azimuth data were digitized manually in their recorded map position. Digital compass-clinometer measurements, automatically georeferenced in the *FieldMove* app (Section 3.1.2), and occasionally corrected, required no further corrections. GCPs defined during TSfM processing (Section 4.2.1) enabled the generation of a spatially correctly referenced virtual outcrop that did not require any further corrections. These three

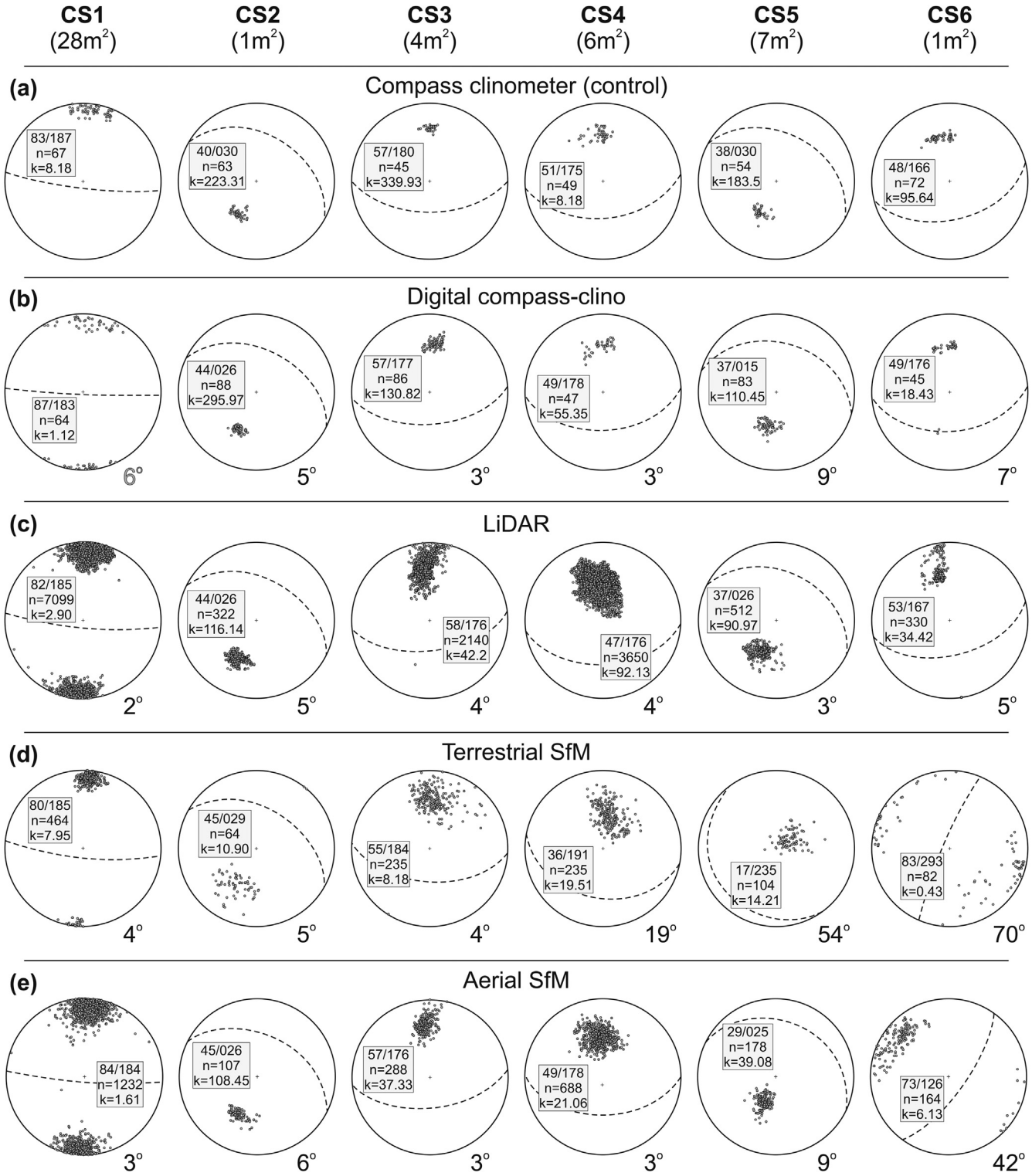


**Fig. 4.** Poles to bedding for control surfaces 1–6 around the study site. Locations of control surfaces in shown in Fig. 2. Plotted great circles denote mean principle orientations for each dataset. Values inside stereonets denote mean principal orientation (dip/dip azimuth), number of measurements and k-values for dispersion of poles to bedding (Fisher et al., 1987). Data for LiDAR, TSfM and ASfM represent triangle orientations for reconstructed meshes. Large bold values at bottom right of stereonets: deviation in degrees of mean principal orientation of planes from control data (traditional compass-clinometer). All stereonets are equal-angle, lower hemisphere projections.

datasets were combined into an oriented geometrical frame in *Move 2016.1 by Midland Valley.*

#### 4.4.1. Accuracy of direct georeferencing and applied corrections

Direct georeferencing of the ASfM point-cloud by use of geotagged imagery in PhotoScan (Section 4.2.2) significantly reduced user input time (Table 1) into the processing workflow. To estimate the efficacy of this process, after importing the ASfM virtual outcrop to *Move,* known points on the virtual outcrop were picked and compared to corresponding dGPS points (Fig. 3d) on the TSfM virtual outcrop, acquired during the TSfM survey (Section 3.2.2). This comparison enabled an approximate estimation of inaccuracies in scale, orientation and position. Table 2 provides a summary of post-processing-applied corrections to the directly georeferenced ASfM virtual outcrop. Calculations from applied corrections provide an estimate of less than 1-degree rotation and a scaling ratio of 1.006 of the virtual outcrops relative to control measurements. For the purposes of this study, this variation was well within accepted ranges of error, given deviations in bedding orientations and user/instrument error in dip and dip azimuth measurements, irrespective of the method used. As such, further investigations into accuracy and precision of direct georeferencing were not required for this study (see James et al., 2017 for detailed study and review).

## 5. Orientation measurement accuracies and virtual outcrop comparisons

After compiling the data into a single georeferenced framework, differences between the five datasets (three virtual outcrops and two sets of direct measurements) were identified by: (1) targeted comparisons of structural measurements from defined control surfaces around the outcrop (Sections 5.1 and 5.2); (2) assessment of differences in point distributions through a single cross-section slice of LiDAR, TSfM and ASfM dense point-clouds (Section 5.3), and (3) coverage and 'completeness' comparisons of the three virtual outcrops (Section 5.4).

### 5.1. Control surfaces

To perform a quantitative comparison of our data collection methods and accuracy of surface reconstruction in virtual outcrops, a number of bedding surfaces around the syncline structure were analyzed (Fig. 2c). This targeted approach provided six defined areas of the outcrop (or virtual counterparts) for measurement comparison. 'Control surfaces' were chosen to represent the range in bedding surface characteristics on the syncline, taking aspect, elevation, size and structural position into account. As such, bedding planes from both the limbs and the hinge of the syncline were chosen for analysis. Overhanging and upward facing planes, those near the base and higher up on the structure, and planes visible from different compass directions were also important considerations when selecting control surface locations (Fig. 1c). Accounting for these factors we selected six control surfaces (CS1-6) that fulfilled all criteria for quantitative comparisons of methodologies.

Multiple direct dip and dip azimuth measurements were collected on each surface using a traditional compass-clinometer (our control dataset). This process was repeated with the FieldMove app on iPad, with a similar number of measurements made for each control surface. After processing and georeferencing of the LiDAR, TSfM and ASfM virtual outcrops, the six control surfaces were manually identified in each virtual outcrop. Patches containing multiple mesh triangles on each control surface were selected and analysed for dip and dip azimuth. The dip and dip azimuth of each mesh triangle in the selected patch is plotted as a pole on an equal angle stereonet (Fig. 4) for comparison with our control data (the traditional compass-clinometer measurements). Spherical statistical methods using an orientation matrix and eigenvectors were then used to calculate mean principal orientations of bedding planes and vector dispersion of poles to bedding (Fisher et al., 1987). They provided us with mean principal dip and dip azimuth data for the mesh triangle populations in each of the six control surfaces for the remotely acquired data, and corresponding orientation measurements collected in the field.

#### 5.1.1. Digital compass-clinometer

Digital compass-clinometer control surface data display a dip deviation of up to 4° with respect to traditional compass-clinometer measurements (Fig. 4). Deviation of dip azimuth, however, is more pronounced. This is especially apparent for CS5 and CS6, which display respective deviations of 10 and 15° from the mean principal orientation of the traditional measurements. In addition, digital compass-clinometer stereonet poles display greater dispersion (and lower K-values) than traditional measurements on the majority of control surfaces. Measurement drift was observed on a number of occasions during fieldwork using *FieldMove* on the iPad, and is particularly pronounced with respect to dip azimuth orientations. User monitoring, censoring of orientation readings and gyroscope updating is required at regular intervals, and calibration against a traditional compass-clinometer is recommended. Restarting the app and hence updating the gyroscope is generally sufficient to rectify any measurement drift, before resuming fieldwork. Poor agreement of dip azimuth data to traditional measurements for CS5 and CS6 is thought to be likely due to measurement drift and insufficient recalibration.

#### 5.1.2. LiDAR control surfaces

LiDAR derived reconstructions display the greatest consistency with compass-clinometer measurements for the six different control surfaces. A maximum deviation from control data of five degrees in mean principal orientation (angular deviation between normals to mean principal orientation) was calculated for control surfaces 2 and 6 (Fig. 4c). High point-cloud densities and detailed LiDAR-mesh reconstruction results in the conservation of bedding plane asperities (Fig. 4c), and thus greater dispersion of poles to bedding than control data. Despite greater pole dispersion, good agreement of data to control measurements and statistical robustness afforded by large sample numbers (Fisher et al., 1987) means that this conservation of bedding plane asperities does not negatively affect mean principal orientations of control surfaces. General agreement of mean principal orientations to control data (Fig. 4) display the fidelity of LiDAR derived mesh reconstructions to true outcrop geometries.

#### 5.1.3. TSfM control surfaces

This method generally yielded the poorest results across all datasets along with the greatest deviation from the control (Fig. 4). TSfM reconstructions of CS1, CS2 and CS3 display good agreement to control data with deviation values similar to the LiDAR dataset, albeit with greater dispersion of plotted poles. Data from CS4, CS5 and CS6, however, display high deviation in mesh triangle orientations, greater dispersion of plotted poles and less reliable reconstructions, when compared to compass-clinometer. The greatest deviation from compass-clinometer, of 70°, occurs at CS6. Also, mean principal orientations of some bedding surfaces (CS4, CS5) have a dip azimuth direction roughly opposite to that of other datasets (Fig. 4). A full discussion of the inaccuracies and variable reliabilities in TSfM reconstructions is provided in Section 7.2.

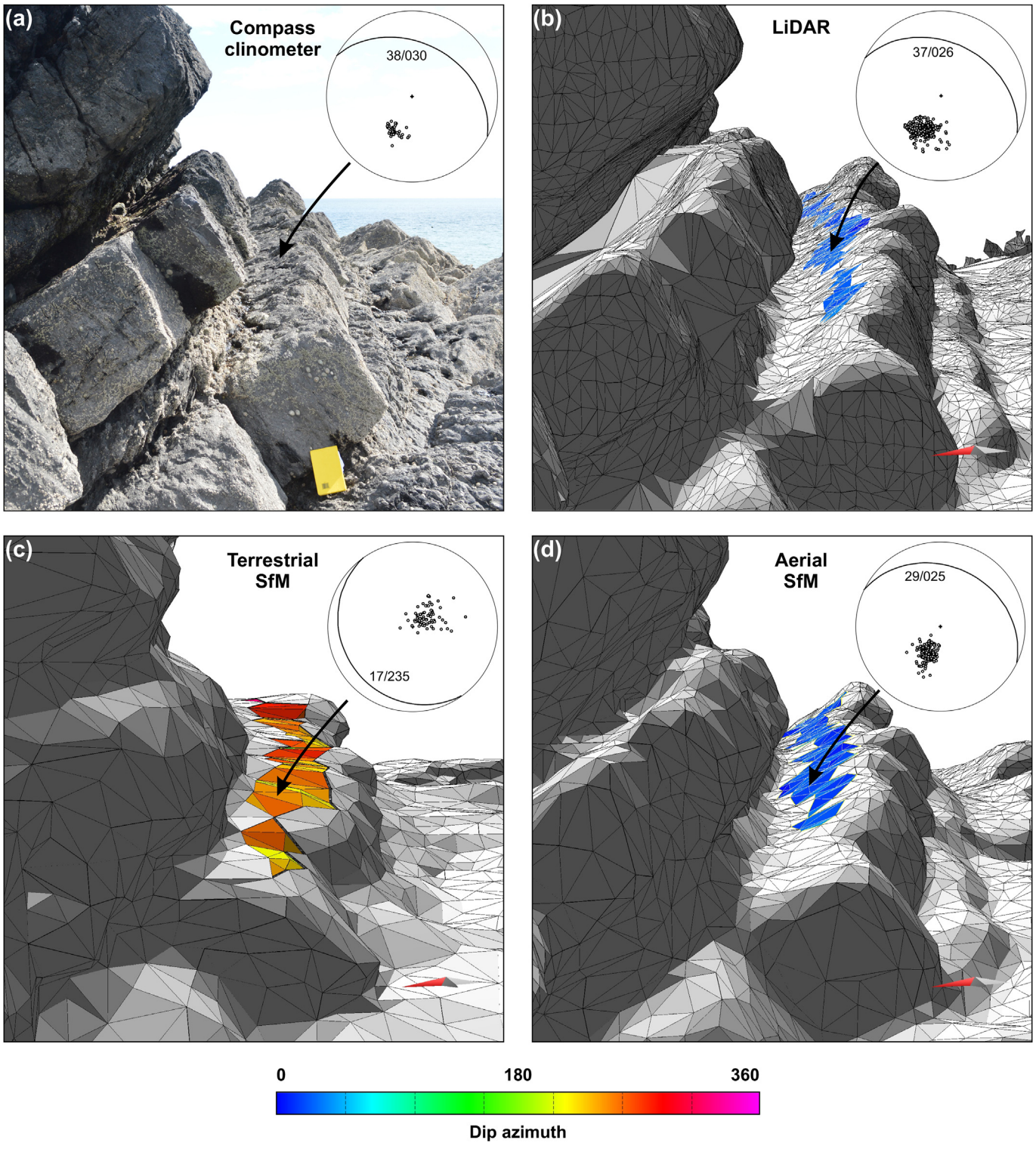


**Fig. 5.** (a) Field photograph of southern part of structure, with CS5 in centre of image, marked by arrow. Notebook 200 mm in height. Detail of triangulated virtual outcrop meshes over CS5 and poles to mesh triangles for (b) LiDAR, (c) TSfM and (d) ASfM, highlighting differences in dip azimuth for surface reconstructions. Great circles and values inside stereonets represent mean principal orientations for measurements (dip/dip azimuth). . Wireframe meshes left untextured for clarity. Detailed data for CS5 provided in Fig. 4. (For interpretation of the references to colour in this figure legend, the reader is referred to the web version of this article.)

*5.1.4. ASfM control surfaces*

Mesh surfaces derived from ASfM were generally of greater accuracy than those derived from TSfM. Reconstructions of CS5 and CS6 display increased deviation from control data, though to a lesser extent than TSfM. Maximum deviation of mean dip and dip azimuth across control surfaces is 25° and 40° respectively. Tighter clustering of poles for ASfM reconstructions indicate greater homogeneity in mesh triangle orientations (Fig. 4) compared to TSfM

and consequently a greater confidence in mean principal orientations. While these data displays some deviation from control, reliability of surface reconstructions is greater than the TSfM dataset.

### 5.2. Control surface 5: a visual appraisal

A detailed view of CS5 (Fig. 5) reveals the discrepancies between surface reconstructions of the three virtual outcrops. The TSfM surface reconstruction (Fig. 5c) has a mean principal dip azimuth in the opposite dip quadrant to that of the other datasets, and visual comparison with the field photograph (Fig. 5a) of the same area shows the mesh surface reconstruction to be erroneous. Though the LiDAR reconstruction for CS5 contains a greater number of mesh triangles (512) than TSfM (104) and ASfM (178) equivalents, and hence orientation measurements, we do not attribute discrepancies in bedding orientations to mesh or measurement density. Inspection of the respective CS5 reconstructions reveals smoothing of the stepped profile and flattening/inversion of the dip panel in the TSfM virtual outcrop (Fig. 5).

### 5.3. Dense point-cloud distributions

Inspection of identically subsampled point-clouds (Fig. 6) from which mesh reconstructions were derived, reveals the differences in datasets. LiDAR point distributions faithfully represent the stepped profile of the structure (see Fig. 1), and the angular nature of bedding edges. In addition, surfaces unsampled by LiDAR are apparent at a number of places through the point-cloud cross-section, where outcrop geometry and low-elevation survey positions placed bedding planes in scan shadow (Fig. 6, inset B). In contrast, TSfM point distributions display a distinctly smoothed trend where topographic recesses are pronounced (Fig. 6, inset C). Surfaces unsampled by LiDAR (Fig. 6, inset B) are populated by TSfM data. Thus, TSfM points are more continuously and evenly distributed across the section than those generated by LiDAR, but are not geometrically representative of the outcrop, particularly where the outcrop profile is angular. ASfM point distribution displays a trend for greater continuity and regularity of point distribution across the section, and a number of surfaces unsampled by terrestrial methods are well sampled by this method (Fig. 6). At some locations across the section (Fig. 6, inset C) minor smoothing across bed edges is apparent in ASfM point distributions, but to a lesser degree than observed in the TSfM data.

Greatest agreement between datasets is observed on large planar or ‘simple’ surfaces, whereas areas of stepped weathering and recessed bedding surfaces result in the greater deviation in point-cloud distributions. As all datasets were meshed using identical parameters, the three separate dense point-clouds underwent the same process of data reduction and point interpolation during processing. Point distribution is the fundamental control on surface reconstruction accuracy, and results from Section 5.2 clearly shows that poor surface reconstructions are coincident with significant point smoothing over areas of stepped outcrop profile. An appraisal of control surface results reveals that the LiDAR dataset is of greater accuracy than TSfM and ASfM counterparts, and as the datasets were meshed using identical parameters, point distribution is the controlling factor. Given that TSfM and LiDAR data in this study were both collected from terrestrial survey stations, point sampling and distribution were expected to be roughly coincident, with occlusion occurring at similar locations. Fig. 6, however, displays marked differences in respective point distributions, the causes for which are addressed in Section 7.

### 5.4. Comparisons of virtual outcrop coverage

Virtual outcrop reconstructions of 69% (LiDAR), 78% (TSfM) and 100% (ASfM) were achieved of the Stackpole structure by the respective remote acquisition techniques. A visual comparison of the three dip azimuth-coloured virtual outcrops (Fig. 7) highlights the differences in coverage and completeness of the reconstructions. Patchy coverage and mesh surfaces with a large number of holes is characteristic of the LiDAR data, while the extent of TSfM is similar, but more complete, in agreement with

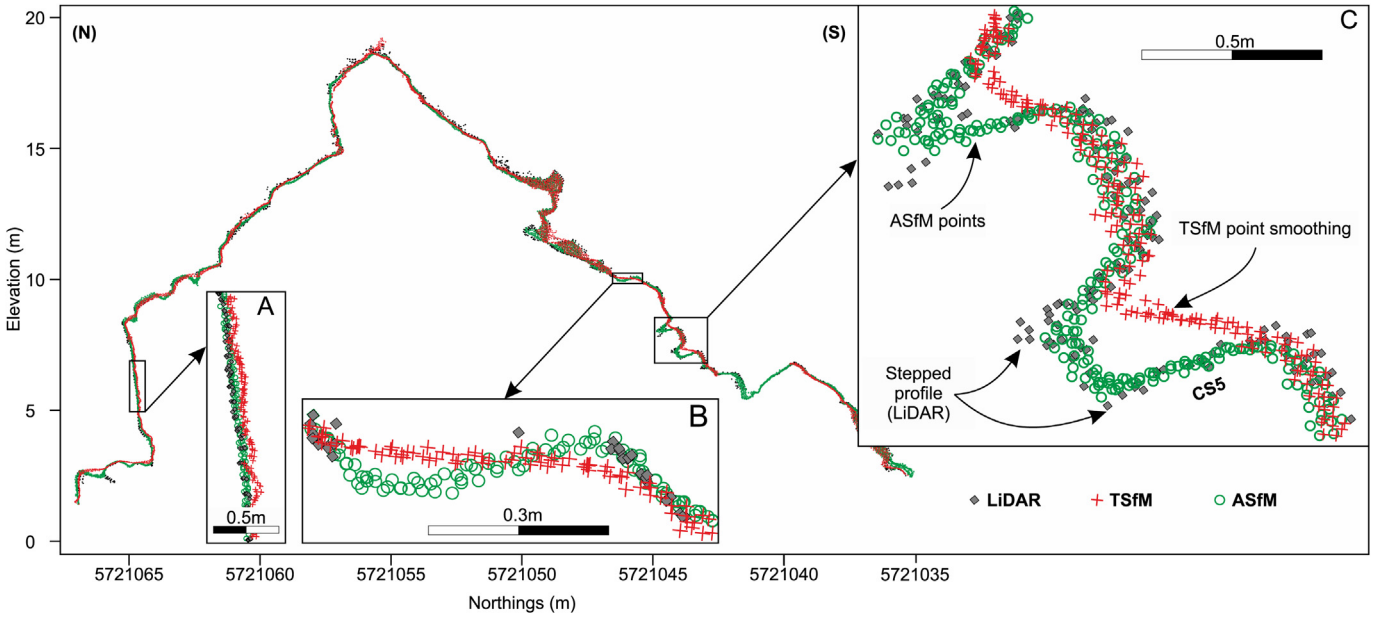


**Fig. 6.** Cross section through point-clouds derived from LiDAR, TSfM and ASfM, showing differences in point distribution. No vertical exaggeration on main section or insert panels. Populations are represented by all points within 0.2 m of section line, oriented 10° NNE. Inset panel at south of section displays systematic differences in point-cloud distributions where outcrop shows stepped profile, particularly with TSfM data. Inset panel at north of the section, on a relatively planar surface, displays greater agreement between datasets, with only minor (~50 mm) offset of TSfM points to the south.

observations from Fig. 6. This effect is due to the lack of suitable survey stations at the seaward side of the structure (Fig. 2c), and a lack of available synoptic vantage points for terrestrial LiDAR scanning and acquisition of images for TSfM around the outcrop. The ASfM virtual outcrop, however, displays complete coverage of the structure, particularly toward the top and eastern end of the outcrop, due to the ability to gain elevated survey positions from the UAV platform (Fig. 3a).

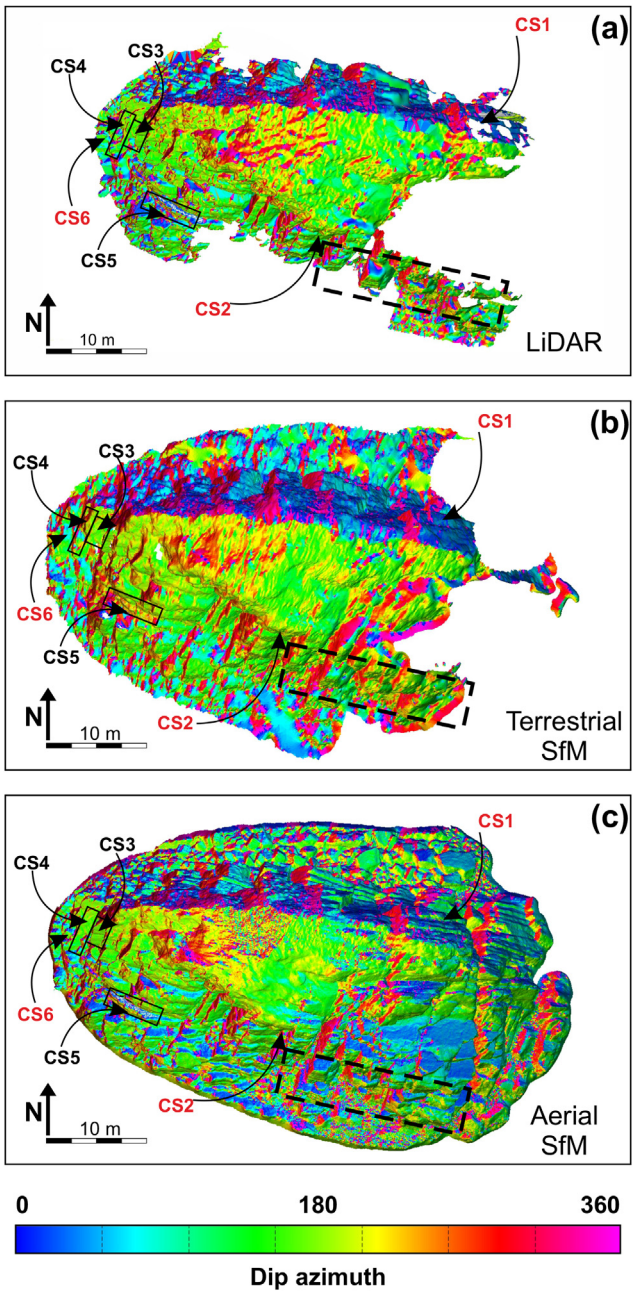


**Fig. 7.** Map view of dip azimuth coloured virtual outcrops using the three remote acquisition techniques for the study. (a) LiDAR; (b) TSfM; (c) ASfM. Control surface locations marked by black arrows. Red text denotes control surfaces not visible in map view, i.e. overhanging beds. Of note is the greater coverage afforded by UAV platform (c) and resultant extent of virtual outcrop, revealing a number of bedding plane reconstructions absent from terrestrial datasets. Dip azimuth colouration facilitates the process of bed 'picking' and selection of surfaces deemed with high confidence to be representative of bedding. The thick dashed box highlights bedding planes toward the top of the structure with dip azimuth to N, clearly picked out in the ASfM dataset (c) but not by terrestrial methods (a) & (b) due to occlusion. (For interpretation of the references to colour in this figure legend, the reader is referred to the web version of this article.)

Colouring the mesh surface for dip azimuth (Fig. 7) highlights corresponding surfaces across the three virtual outcrops datasets that do not have the same orientation attributes. This difference is clear on the southeastern part of the mesh reconstructions (Fig. 7b, dashed box), where NE-dipping surfaces (coloured blue) are faithfully represented by LiDAR and ASfM, but TSfM counterparts appear to be SW-dipping (coloured red). This highlights the trend in the TSfM dataset for erroneous mesh reconstructions, as observed on CS5 (Fig. 5).

## 6. Geological model building from structural data

Direct comparisons of surface reconstructions and directly acquired data provide an insight into the limitations of contrasting surveying methods and potential sources of error. Part of the aim of this study was to ascertain how these factors ultimately impact structural interpretation and model building. To test this, we calculate fold-projection vectors based on established methods (Ramsay and Huber, 1987) to predict the along strike position of the syncline hinge and the fold geometry.

### 6.1. Orientation data acquisition

In addition to the data acquired for control surface comparisons, orientation data were collected across the entire structure during fieldwork by compass-clinometer (traditional & digital), and subsequently, from virtual outcrops. As with field collection of data, the LiDAR, TSfM and ASfM virtual outcrops were examined separately, and only surfaces that were deemed as representative of bedding were targeted for data collection and analysis. Mean principal orientations were calculated from these mesh triangle patches and used to populate stereonets for fold axis calculations (Fig. 8). Each plotted data point in Fig. 8 (c, d and e) represents the mean principal orientation of a picked bedding patch on the respective LiDAR, TSfM or ASfM virtual outcrops.

Of the models generated in this study, the most complete virtual outcrop was afforded by the UAV platform (Fig. 7) and provided the greatest number of measureable bed surfaces. Most critically, top bedding surfaces on the southern face of the structure (dipping to the NE and coloured blue, Fig. 7c) were picked with much greater confidence than on the terrestrially acquired counterparts. Virtual outcrop holes associated with low-elevation LiDAR acquisition and errors in TSfM surface reconstructions were common (Figs. 5 and 6; Sections 7.1 and 7.2), particularly on higher, upward facing beds. Consequently, picking LiDAR bed reconstructions was difficult over some parts of the outcrop, and a number of TSfM surfaces were rejected, based on quality checking of orientation data. Overhanging surfaces (i.e. bed bases) provided the bulk of the measurements on the southern side of the outcrop from terrestrially acquired datasets (e.g. CS1, CS2 & CS6; Fig. 2). Due to the data acquisition angle (upward), these overhanging surfaces provided the most reliable reconstructions of true bedding. The numbers of poles to bedding on fold projection stereonets (Fig. 8) reflect the number of 'patches' confidently picked for data extraction, from which mean principal orientations were calculated.

### 6.2. Fold axes calculations from orientation data

Following extraction of bed orientation data from the virtual outcrops, each dataset, including those directly collected (traditional and digital), were plotted as poles to bedding (Fig. 8) for the purpose of structural analysis. High-density CS data points were not included at this stage to ensure statistically representative

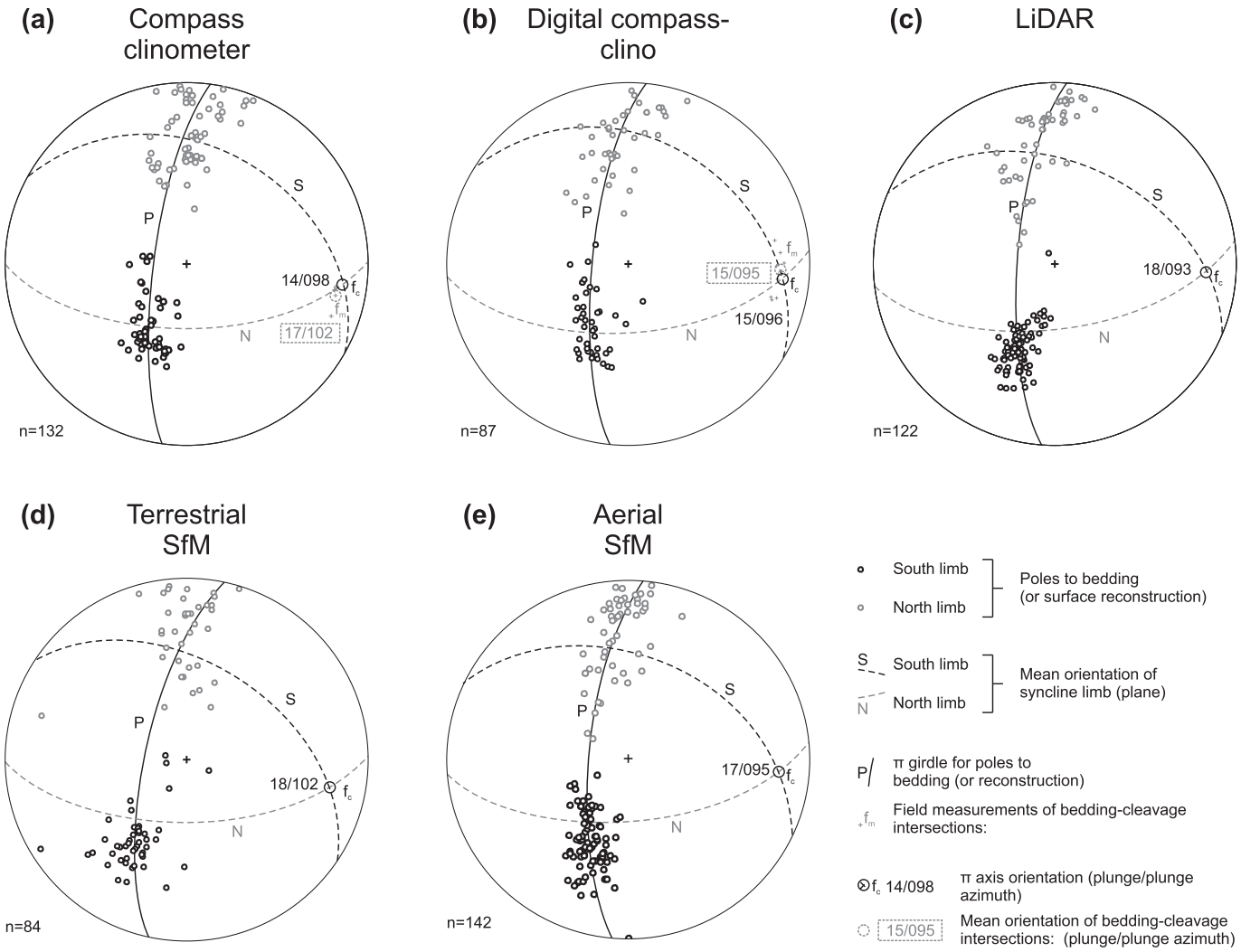


**Fig. 8.** Poles to bedding (or surface reconstruction), calculated π-girdles, π-axes and fold limbs for the five acquisition methods. All projections on equal-angle lower hemisphere stereonets.

samples (Fisher et al., 1987). Best-fit great circles (i.e. π-girdles) (Ramsay and Huber, 1987) were calculated for each dataset. Derived π-axes (normal to π-girdles) were plotted and recorded to predict fold axis orientation. This method was chosen as a means of contrasting the effects of different data acquisition methods on along-strike prediction from structural models. In addition, field measurements of bedding-fracture intersection lineations, interpreted as fold-axis parallel, were included in Fig. 8 for comparison with calculated values.

Poles to fold limbs, π-girdles and π-axes for each of the five datasets display similar trends on first appraisal (Fig. 8). On closer inspection, pole distributions reveal some important differences, particularly with respect to pole density. Pole to bedding distribution is similar for traditional compass-clinometer, digital compass-clinometer and ASfM, with fairly even distribution of points on and around the π-girdle, including in the hinge zone of the syncline. TSfM and LiDAR data reveal a paucity of poles in the hinge (Fig. 8c and d) and a roughly bimodal distribution. Greater dispersion of poles is evident in the TSfM dataset throughout both limbs and hinge of the syncline, with occasionally points falling far outside of the range represented by the other datasets. Of the remotely acquired data, ASfM and LiDAR poles display greater similarity to those from direct measurements, although with differences in azimuth and plunge of calculated fold axes. Fold axis calculations from the two directly measured datasets (Fig. 8a and c) show the least deviation between each other, of 1 and 3° for dip and dip azimuth respectively. Finally, the TSfM fold axis shows the greatest deviation from traditional compass-clinometer (control data).

### 6.3. Cross sections and along-strike deviation

Projection of the predicted fold geometry onto serial cross sections allowed a quantification of along-strike deviation of the fold hinge using calculated fold axes from bedding orientations for each dataset. To begin with, a single bedding surface, identifiable on both limbs and the hinge at the western end of the structure was mapped and digitized as a polyline in 3D space. This feature was detected in all three virtual outcrops (LiDAR, TSfM & ASfM) and clearly visible in the field. Because of the limited extent of the Stackpole structure, the fold was assumed to be cylindrical and calculated fold axes (Fig. 8) were used as projection vectors (Ramsay and Huber, 1987) onto 12 serial cross sections (Fig. 2d) striking 10° NNE, spaced 5 m apart. The projection of the same single polyline onto cross sections removed interpretational bias and allowed a direct comparison of data acquisition methods. Polyline node deviation was calculated using 2D Root Mean Square Error on the *y* (northing) and *z* (elevation) plane, adapted from calculations for horizontal map accuracy using remotely sensed

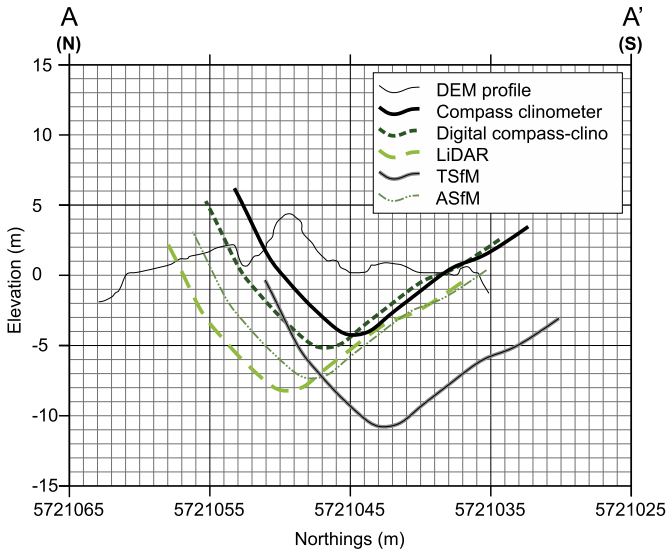


**Fig. 9.** Projected polyline interpretation to section A-A′ (see section location Fig. 2d). Cross-section shows the projection of a single interpretation of a bedding surface at the NW end of the outcrop using five different fold axis orientations. The graph highlights the along-strike divergence, resulting from the fold axis predictions based on data collected by the different acquisition methods.

data (Congalton and Green, 2008).

Calculated fold profiles from poles to bedding (Fig. 8) and resultant projections of polylines to cross section (Fig. 9) highlight the rapid divergence of predictions over a short distance (60 m) along strike. RMS calculations of fold hinge nodes for different acquisition methods show deviation from control of 2.1 m for digital compass-clinometer, 4.3 m for ASfM, 6.4 m for LiDAR and 6.9 m for TSfM predictions respectively, at 60 m projection distance from polyline interpretation (Fig. 10).

## 7. Remote acquisition methods and effects on along-strike prediction

### 7.1. Terrestrial LiDAR

Terrestrial LiDAR derived surface reconstructions were of greater accuracy than SfM equivalents, and show greater agreement to direct measurements (Fig. 3). Given these high accuracy reconstructions, derived along-strike predictions were expected to be most similar to those derived from control data (compass-clinometer measurements). Examination of these along-strike predictions (Figs. 8–10), however, shows that with the exception of TSfM, LiDAR predictions diverge from control to a greater degree (Figs. 9 and 10) than the other measurement methods (remote or direct). The relatively poor coverage of the LiDAR virtual outcrop (Fig. 7) and associated lack of surfaces or patches from which to extract orientation data during interpretation resulted in under-sampling of parts of the syncline structure (see Fig. 8 for stereonet data).

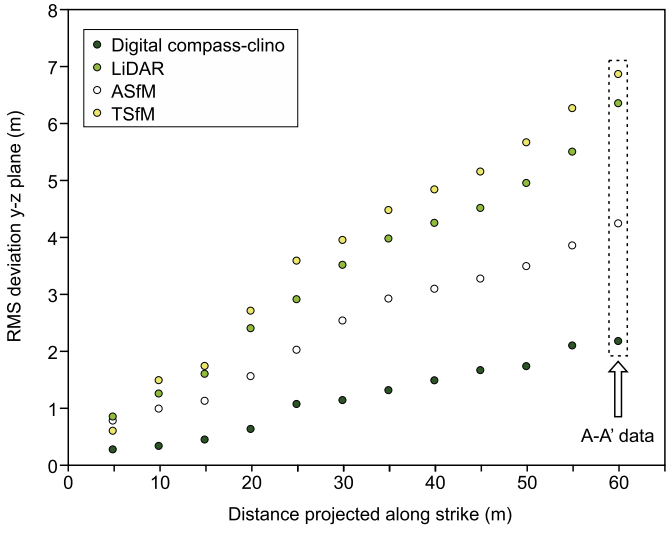


**Fig. 10.** RMS deviation of polyline nodes relative to control (compass-clinometer), at 12 cross section locations from E-W. All sections oriented N-S. Deviation in 2D (northing (y) - vertical (z) plane).

This behaviour resulted in a paucity of measurements (Fig. 8) in this structurally important area, and thus greater deviation from control in along-strike prediction. This issue arises primarily because the structure is an upright, ENE-plunging synform, and as such bedding planes dip toward the centre of the structure, and gently seaward. Survey positions above, and to the seaward side of the outcrop are thus best at this site, particularly for bedding planes in the hinge of the syncline. Terrestrial survey positions did not provide sufficient elevation to reconstruct the hinge zone, and in an attempt to reduce the effects of occlusion, elevated positions (~60 m from the outcrop) were chosen during field acquisition.

As such, predictions using the LiDAR dataset were less constrained than those from ASfM and direct measurements (traditional & digital), particularly in the hinge zone of the syncline (Fig. 8). The schematic presented in Fig. 11a highlights the high accuracy of LiDAR reconstructions where bedding planes are visible to terrestrial scan stations, but the limiting effects on reconstruction where occluded. It should be noted that, in contrast to SfM, single LiDAR scans of surfaces provided sufficient data (e.g. CS5, Fig. 5) to generate highly accurate surface reconstructions, whereas at least two aligned images, but preferably more, are required for SfM reconstructions. This consideration is an important one, and a factor that significantly affected the accuracy of TSfM reconstructions.

### 7.2. TSfM: partial occlusion, low image resolution and reconstruction errors

TSfM derived along-strike predictions reflect the negative effects of occlusion in two ways. First, as with the LiDAR virtual outcrop, large parts of the outcrop are not represented by reconstructions, and thus bedding surfaces were not sampled, particularly in the hinge zone of the syncline. Second, where bedding planes were *partially occluded* to TSfM camera positions, surfaces are reconstructed erroneously. Given the improved accuracy of SfM reconstructions with higher overlapping image counts (see Section 4.2), this partial occlusion is a major factor to be considered during acquisition. An appraisal of image overlap numbers reveals that between 2 and 9 overlapping images were used for generating each tie-point during TSfM processing (compared to between 6 and 12 for ASfM). An example of this effect is provided by poor TSfM surface reconstruction of CS5 (see Figs. 4–6). While this bedding plane was not entirely occluded during TSfM acquisition, inspection of terrestrially acquired imagery reveals that CS5 appears in only two images. Point coordinate estimation, therefore, was performed on the minimum number of images required for this part of the outcrop.

Pixel resolution of images used for tie-point matching influences precision of point matching (see Section 4.2) and must be considered to achieve close range, in-focus imagery. Appraisal of TSfM survey positions (Fig. 2a and c) highlights the relatively large distances of terrestrial camera positions from the outcrop,

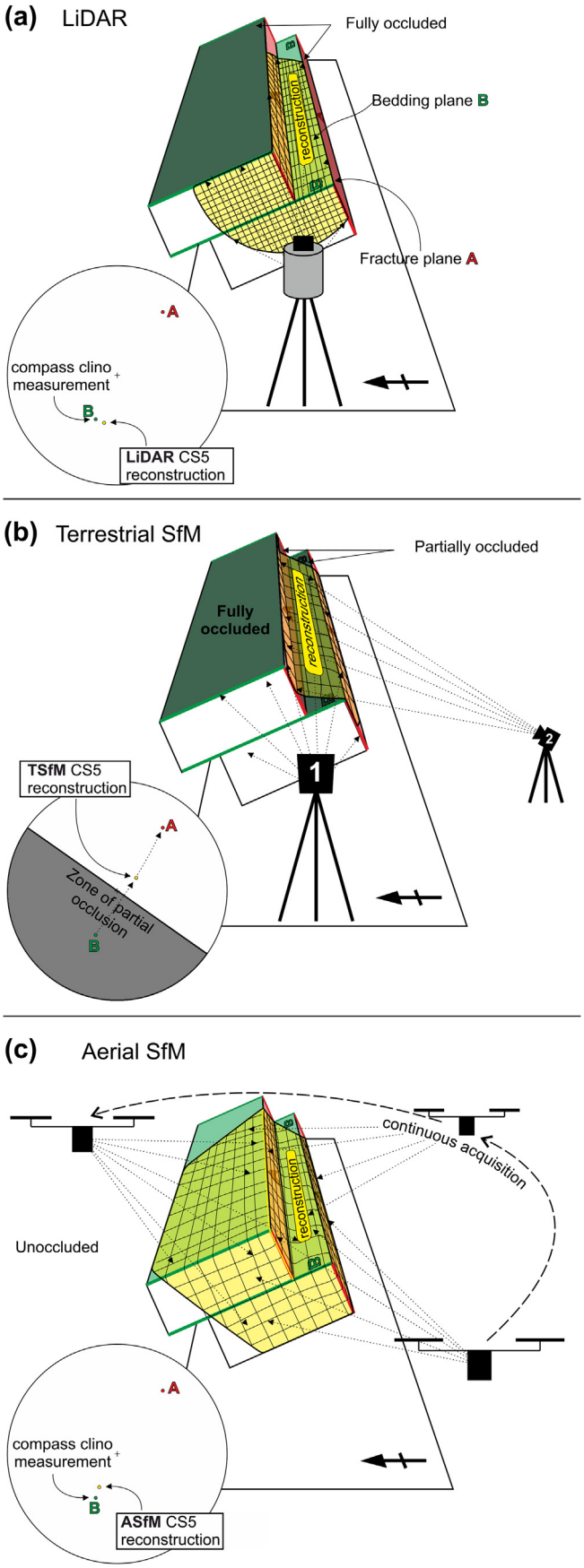


compared to those achieved by UAV (Fig. 3a). These terrestrial positions around Stackpole syncline are fundamentally controlled by local topography, with semi-synoptic viewpoints only available ~60 m from the structure (Fig. 2c). This increased distance from outcrop resulted in a reduced ground-pixel resolutions for TSfM images (7.48 mm average) than for the ASfM dataset (6.24 mm average), in spite of greater camera resolution (see Table 1). This low-resolution imagery is likely to have compounded the negative effects of partial occlusion and further impacted the accuracy of surface reconstructions. This distance-to-outcrop effect did not significantly affect the terrestrial LiDAR dataset, however, given the quoted accuracy, precision and range (see Section 3.2.1) of the instrument used in this study.

These factors had important effects on the accuracy of the final TSfM virtual outcrop and derived along-strike predictions. Full occlusion to terrestrial camera positions at the eastern end of the structure resulted in fewer bedding planes being reconstructed in the hinge of the syncline, and partial occlusion in some places resulted in erroneous bedding reconstructions. The negative outcomes were reduced availability of bedding planes from which to extract structural data, and increased inaccuracies, along with weaker picking confidence, in extracted structural data. These factors likely explain the rapid along-strike deviation from control (Figs. 9 and 10).

### *7.3. ASfM: improved accuracy and coverage from synoptic camera positions*

ASfM achieved along-strike prediction closest to those derived using direct measurements. While this dataset still displays along-strike divergence, it is significantly less than for the other two remote acquisition methods. On individual control surfaces, however, ASfM did not achieve as high control surface accuracy as LiDAR. The ability to move around the study site from a UAV platform allowed close range imagery to be acquired of the outcrop from a number of angles. This manoeuvrability, and the requirement of accurate SfM reconstructions for convergent imagery is a key advantage of a UAV platform over terrestrial image acquisition at this location. The greater coverage afforded by this method allowed a much greater number of reliably reconstructed surfaces to be sampled.

Not only were more bedding planes reconstructed, particularly toward the top and eastern part of the outcrop, but the increased image overlap, improved ground-pixel resolution and convergence of acquisition stations afforded by the manoeuvrable UAV platform meant that reconstructions were more accurate than TSfM. Between 6 and 12 overlapping images were used to automatically

**Fig. 11.** Schematic of acquisition method limitations and effects on surface reconstructions. Bedding plane (B) in green; Fracture plane orthogonal to bedding (A) in red; reconstructions in yellow. Stereonet data represents poles to mean principal orientation of CS5 mesh triangles (See Figs. 4 and 5) for respective acquisition methods (yellow), control CS5 bedding data (green) and fracture plane orientation, measured by compass-clinometer (red). Occluded surfaces shaded grey. (a) LiDAR acquisition from a single scan station. High point density and accurate surface reconstruction over a limited area. Occluded surfaces not reconstructed. Pole to surface reconstruction shows good agreement to control data (true bedding orientation) in green. (b) Terrestrial Structure from Motion from two image acquisition stations. Partial occlusion of target surface (B) results in erroneous surface reconstruction and 'migration' of pole to reconstruction from surface B to surface A by a smoothing effect. Shaded area on stereonet represents area of partial occlusion where surface B is occluded to image station 2. (c) Greater coverage afforded by UAV acquisition and greater completeness of reconstruction as a result. Aerial acquisition allows a greater number of overlapping images to be acquired and thus improves SfM reconstructions. While some smoothing of surfaces occurs at bed edges, reconstruction is of greater accuracy than TSfM counterpart and comparable to LiDAR. (For interpretation of the references to colour in this figure legend, the reader is referred to the web version of this article.)

estimate each ASfM tie-point location (compared to between 2 and 9 for TSfM) and UAV image acquisition points averaged a distance of 13 m from the structure, improving ground-pixel resolution. Bedding planes were also picked and sampled with greater confidence on the ASfM virtual outcrop, such that the entire syncline could be sampled, through both limbs and hinge, as well as along strike, resulting in a better fold axis prediction than either of the other remote acquisition techniques. The 'fullness' of the dataset is likely the cause of the better results and greater agreement with directly collected data, notwithstanding some minor inaccuracies in surface reconstruction. A schematic representation of the advantages of UAV acquisition of images for SfM reconstruction is provided in Fig. 10c.

## 8. Discussion

This case study at Stackpole Quay demonstrates how different acquisition techniques and outcrop morphology have important effects on structural analysis, not only through the accuracy of derived structural data, but also the amount and distribution of the data that each method provides. Accurately reconstructed bedding planes by terrestrial LiDAR did not automatically provide accurate along-strike predictions in this case, primarily because structurally important, data-rich parts of the outcrop were not sampled. Similarly, the Terrestrial Structure from Motion dataset suffered from the negative effects of occlusion, where large parts of the outcrop were un-reconstructed. This outcome is an effect of the characteristic morphology of Stackpole Quay, and the lack of close range, synoptic survey points around the structure. The ability to survey the entire outcrop aerially, however, provided the camera positions and angles to fully reconstruct the outcrop and thus derive structural data from any chosen bedding plane. This clear advantage of UAV acquisition has particular influence on structural models from Stackpole, given the fact that the structure is an upright syncline, with inward-dipping beds.

The availability and accuracy of structural data proved important for along-strike predictions. Where a paucity of data existed, as in the LiDAR and TSfM reconstructions, structural predictions were poorly constrained. Where bedding planes were partially occluded to terrestrial camera positions, erroneous reconstruction of surfaces led to greater variability of structural data and difficulties in picking bedding planes for data extraction with confidence. The quality of virtual outcrops is thus critical if reliable structural data are to be extracted from them. This requirement implies that careful consideration should be given to every stage of the process, from survey planning, data acquisition and processing to the extraction of structural data and the ways in which predictions are made. During survey planning and acquisition of data for virtual outcrop construction by SfM, attention should be paid to the principles of this technique, and survey design should account for the requirement of SfM for close range, convergent, overlapping imagery. Differences in lighting of surfaces or features displaying low contrast can negatively impact SfM reconstructions through the inability to match features and generate tie-points, and as such timing of surveys should be considered.

Irrespective of the acquisition technique, quality checking of models is prudent to ensure reliable results are obtained. The collection of ground-truth data, in the form of dGPS control points and measured bedding orientations at the study site enables calibration of remotely acquired data, and can aid in analysis and interpretation. Data assessment during SfM processing is critical: consideration should be given to overlapping image numbers, tie-point image counts, accuracy of tie-point estimations, and relative point densities. Chosen processing parameters are likely to be determined by the specific requirements of the study, but where this primary data do not meet predetermined thresholds, derived structural measurements and predictions should be treated with circumspection. These quality checks are important to improve virtual outcrop accuracy, reduce uncertainty and ultimately make better geological predictions using modern techniques.

## 9. Conclusions

This case study from Stackpole Quay highlights the relative merits and shortcomings of modern versus traditional techniques for structural measurement and along-strike prediction. UAV image acquisition coupled with SfM software generated a virtual outcrop that provided better along-strike predictions than terrestrial LiDAR and terrestrial SfM counterparts. While LiDAR surface reconstructions proved more accurate than either SfM dataset, the greater coverage afforded by UAV allowed improved characterisation of the structural geometry of the study site, and thus provided a better predictor of along strike structure. This result reflects the morphology of the study site and the level of accuracy required for predictive geological modelling. Irrespective of the characteristics of the individual study site or the methodology used, careful survey planning, data processing, and quality checking of this data is critical for robust structural analysis and accurate geological models.

## Acknowledgements

This study was carried out as part of a University of Aberdeen provided PhD supported by The NERC Centre for Doctoral Training in Oil & Gas, (grant reference: NE/M00578X/1). Thanks to Magda Chmielewska for her training and help with LiDAR processing, without which this study could not have been undertaken. Midland Valley Exploration is thanked for academic use of Move 2016 software. We gratefully acknowledge the detailed and constructive reviews by Mike James and an anonymous reviewer, and thanks to Bill Dunne for careful and thorough editorial comments, all of which greatly improved the manuscript.

## Appendix A. Supplementary data

Supplementary data related to this article can be found at http://dx.doi.org/10.1016/j.jsg.2017.04.004.

## References

Assali, P., Grussenmeyer, P., Villemin, T., Pollet, N., Viguier, F., 2014. Surveying and modeling of rock discontinuities by terrestrial laser scanning and photogrammetry: semi-automatic approaches for linear outcrop inspection. J. Struct. Geol. 66, 102–114.

Bates, K.T., Rarity, F., Manning, P.L., Hodgetts, D., Vila, B., Oms, O., Galobart, À., Gawthorpe, R.L., Galobart, a., Gawthorpe, R.L., 2008. High-resolution LiDAR and photogrammetric survey of the Fumanya dinosaur tracksites (Catalonia): implications for the conservation and interpretation of geological heritage sites. J. Geol. Soc. 165, 115–127.

Bemis, S.P., Micklethwaite, S., Turner, D., James, M.R., Akciz, S., Thiele, S.T., Bangash, H.A., Thiele S, T., Bangash, H.A., 2014. Ground-based and UAV-based photogrammetry: a multi-scale, high-resolution mapping tool for structural geology and paleoseismology. J. Struct. Geol. 69, 163–178.

Bistacchi, A., Balsamo, F., Storti, F., Mozafari, M., Swennen, R., Solum, J., Tueckmantel, C., Taberner, C., 2015. Photogrammetric digital outcrop reconstruction, visualization with textured surfaces, and three-dimensional structural analysis and modeling: innovative methodologies applied to fault-related dolomitization (Vajont Limestone, Southern Alps, Italy). Geosphere 11, 2031–2048.

Bitelli, G., Dubbini, M., Zanutta, A., 2004. Terrestrial laser scanning and digital photogrammetry techniques to monitor landslide bodies. International Archives of Photogrammetry. Remote Sens. Spatial Inf. Sci. 35 (B5), 246–251.

Bonnaffe, F., Jennette, D., Andrews, J., 2007. A method for acquiring and processing ground-based lidar data in difficult-to-access outcrops for use in three-dimensional, virtual-reality models. Geosphere 3, 501–510.

British Geological Survey, 1996. Tectonic Map of Britain, Ireland and Adjacent Areas.

British Geological Survey, Keyworth, Nottingham.
Buckley, S., Howell, J., Enge, H., Kurz, T., 2008. Terrestrial laser scanning in geology: data acquisition, processing and accuracy considerations. J. Geol. Soc. 165, 625–638.
Buckley, S.J., Schwarz, E., Terlaky, V., Howell, J.A., 2010. Combining aerial photogrammetry and terrestrial lidar for reservoir analog modeling. Photogrammetric Eng. Remote Sens. 76 (8), 953–963.
Casini, G., Hunt, D.W., Monsen, E., Bounaim, A., 2016. Fracture characterization and modeling from virtual outcrops. AAPG Bull. 100 (1), 41–61.
Clapuyt, F., Vanacker, V., Van Oost, K., 2016. Reproducibility of UAV-based earth topography reconstructions based on Structure-from-Motion algorithms. Geomorphology 260, 4–15.
Congalton, R.G., Green, K., 2008. Assessing the Accuracy of Remotely Sensed Data: Principles and Practices. CRC Press.
Coward, M.P., Smallwood, S., 1994. An interpretation of the Variscan tectonics of SW Britain. Geol. Soc. Lond. Special Publ. 14 (1), 89–102.
Dixon, E.E.L., 1921. The Geology of the South Wales Coalfield. Part 13, the Country Around Pembroke and Tenby: Being an Account of the Region Comprised in Sheets 244 and 245 of the Map. H.M.S.O, London.
Downes, J., 2002. Geological Observations in the Dinantian Rocks of the South Pembrokeshire Coastline. Open University Geological Society Journal Spring. Edition 2005.
Eide, C.H.E., Howell, J.A., 2014. Distribution of discontinuous mudstone beds within wave-dominated shallow-marine deposits: star Point and Blackhawk Formations, eastern Utah. AAPG Bull. 98 (7), 1401–1429.
Enge, H.D., Buckley, S.J., Rotevatn, A., Howell, J.A., 2007. From outcrop to reservoir simulation model: workflow and procedures. Geosphere 3, 469–490.
Enge, H.D., Howell, J.A., Buckley, S.J., 2010. Quantifying clinothem geometry in a forced-regressive river-dominated delta, Panther Tongue Member, Utah, USA. Sedimentology 57 (7), 1750–1770.
Fabuel-Perez, I., Hodgetts, D., Redfern, J., 2010. Integration of digital outcrop models (DOMs) and high resolution sedimentology–workflow and implications for geological modelling: Oukaimeden Sandstone Formation, High Atlas (Morocco). Pet. Geosci. 16 (2), 133–154.
Fisher, N.I., Lewis, T., Embleton, B.J.J., 1987. Statistical Analysis of Spherical Data. Cambridge University Press.
Fonstad, M.A., Dietrich, J.T., Courville, B.C., Jensen, J.L., Carbonneau, P.E., 2013. Topographic structure from motion: a new development in photogrammetric measurement. Earth Surf. Process. Landforms 38, 421–430.
Furukawa, Y., Ponce, J., 2010. Accurate, dense, and robust multiview stereopsis. IEEE Trans. Pattern Anal. Mach. Intell. 32 (8), 1362–1376.
García-Sellés, D., Falivene, O., Arbués, P., Gratacos, O., Tavani, S., Muñoz, J.A., 2011. Supervised identification and reconstruction of near-planar geological surfaces from terrestrial laser scanning. Comput. Geosci. 37 (10), 1584–1594.
Gillespie, P., Monsen, E., Maerten, L., Hunt, D., Thurmond, J., Tuck, D., 2011. Fractures in carbonates: from digital outcrops to mechanical models. Outcrops revitalized—tools, techniques and applications: Tulsa, Oklahoma. SEPM Concepts Sedimentol. Paleontol. 10, 137–147.
Gold, P.O., Cowgill, E., Kreylos, O., Gold, R.D., 2012. A terrestrial lidar-based workflow for determining three–dimensional slip vectors and associated uncertainties. Geosphere 8, 431–442.
Hancock, P., 1979. Editorial: background to the journal. J. Struct. Geol. 1, 1–3.
Hancock, P.L., 1964. The relations between folds and late-formed joints in South Pembrokeshire. Geol. Mag. 101 (02), 174–184.
Hirschmuller, H., 2008. Stereo processing by semiglobal matching and mutual information. IEEE Trans. pattern Anal. Mach. Intell. 30 (2), 328–341.
Hodgetts, D., Drinkwater, N.J., Hodgson, J., Kavanagh, J., Flint, S.S., Keogh, K.J., Howell, J.A., 2004. Three-dimensional geological models from outcrop data using digital data collection techniques: an example from the Tanqua Karoo depocentre, South Africa. Geol. Soc. Lond. Spec. Publ. 239, 57–75.
James, M.R., Robson, S., 2012. Straightforward reconstruction of 3D surfaces and topography with a camera: accuracy and geoscience application. J. Geophys. Res. Earth Surf. 117 (F3).
James, M.R., Robson, S., d'Oleire-Oltmanns, S., Niethammer, U., 2017. Optimising UAV topographic surveys processed with structure-from-motion: ground control quality, quantity and bundle adjustment. Geomorphology 280, 51–66.
Javernick, L., Brasington, J., Caruso, B., 2014. Modeling the topography of shallow braided rivers using Structure-from-Motion photogrammetry. Geomorphology 213, 166–182.
Jones, R.R., McCaffrey, K.J., Wilson, R.W., Holdsworth, R.E., 2004. Digital field data acquisition: towards increased quantification of uncertainty during geological mapping. Geol. Soc. Lond. Spec. Publ. 239 (1), 43–56.
Jones, R.R.R., Kokkalas, S., McCaffrey, K.J.W.J.W., 2009. Quantitative analysis and visualization of nonplanar fault surfaces using terrestrial laser scanning (LIDAR)—the Arkitsa fault, central Greece, as a case study. Geosphere 5, 465–482.
Lee, L., Jones, M., Ridenour, G.S., Testa, M.P., Wilson, M.J., 2015. Investigating and comparing spatial accuracy and precision of GPS-enabled devices in middle Tennessee. In: Bian, F., Xie, Y., Cui, X., Zeng, Y. (Eds.), Geo-informatics in Resource Management and Sustainable Ecosystem. Springer, pp. 215–224.
Mancini, F., Dubbini, M., Gattelli, M., Stecchi, F., Fabbri, S., Gabbianelli, G., 2013. Using unmanned aerial vehicles (UAV) for high-resolution reconstruction of topography: the structure from motion approach on coastal environments. Remote Sens. 5 (12), 6880–6898.
Martín, S., Uzkeda, H., Poblet, J., Bulnes, M., Rubio, R.R., 2013. Construction of accurate geological cross-sections along trenches, cliffs and mountain slopes using photogrammetry. Comput. Geosci. 51, 90–100.
Midland Valley, 2015. FieldMove User Guide.
Novakova, L., Pavlis, T.L., 2017. Assessment of the precision of smart phones and tablets for measurement of planar orientations: a case study. J. Struct. Geol. 97, 93–103.
Pringle, J.K., Howell, J.A., Hodgetts, D., Westerman, A.R., Hodgson, D.M., 2006. Virtual outcrop models of petroleum reservoir analogues: a review of the current state-of-the-art. First break 24 (3), 33–42.
Ramsay, J.G., Huber, M.I., 1987. The Techniques of Modern Structural Geology: Folds and Fractures. Academic Press.
Rarity, F., van Lanen, X.M.T., Hodgetts, D., Gawthorpe, R.L., Wilson, P., Fabuel-Perez, I., Redfern, J., 2014. LiDAR-based digital outcrops for sedimentological analysis: workflows and techniques. Geol. Soc. Lond. Spec. Publ. 387, 153–183.
RIEGL, 2015. Data Sheet, RIEGL VZ-2000.
Rittersbacher, A., Howell, J.A., Buckley, S.J., 2014. Analysis of fluvial architecture in the Blackhawk Formation, Wasatch Plateau, Utah sing large 3D photorealistic models. J. Sediment. Res. 84, 72–87.
Rotevatn, A., Buckley, S.J., Howell, J.A., Fossen, H., 2009. Overlapping faults and their effect on fluid flow in different reservoir types: a LIDAR-based outcrop modeling and flow simulation study. AAPG Bull. 93, 407–427.
Seers, T.D., Hodgetts, D., 2014. Comparison of digital outcrop and conventional data collection approaches for the characterization of naturally fractured reservoir analogues. Geol. Soc. Lond. Spec. Publ. 374 (1), 51–77.
Seitz, S.M., Curless, B., Diebel, J., Scharstein, D., Szeliski, R., 2006 June. A comparison and evaluation of multi-view stereo reconstruction algorithms. In: Computer Vision and Pattern Recognition, 2006 IEEE Computer Society Conference on (Vol. 1, 519–528). IEEE.
Sturzenegger, M., Stead, D., 2009. Quantifying discontinuity orientation and persistence on high mountain rock slopes and large landslides using terrestrial remote sensing techniques. Nat. Hazards Earth Syst. Sci. 9 (2), 267–287.
Tavani, S., Granado, P., Corradetti, A., Girundo, M., Iannace, A., Arbués, P., Muñoz, J.A., Mazzoli, S., 2014. Building a virtual outcrop, extracting geological information from it, and sharing the results in Google Earth via OpenPlot and Photoscan: an example from the Khaviz Anticline (Iran). Comput. Geosci. 63, 44–53.
Vasuki, Y., Holden, E.-J.J., Kovesi, P., Micklethwaite, S., 2014. Semi-automatic mapping of geological Structures using UAV-based photogrammetric data: an image analysis approach. Comput. Geosci. 69, 22–32.
Westoby, M.J., Brasington, J., Glasser, N.F., Hambrey, M.J., Reynolds, J.M., 2012. "Structure-from-Motion"photogrammetry: a low-cost, effective tool for geoscience applications. Geomorphology 179, 300–314.